IEEE Access
Multidisciplinary | Rapid Review | Open Access Journal

Received 20 August 2024, accepted 30 August 2024, date of publication 9 September 2024, date of current version 17 September 2024.

Digital Object Identifier 10.1109/ACCESS.2024.3454519

RESEARCH ARTICLE

Simulation and Fabrication Feasibility of Two-Channel All-Optical Modulator Exploiting InAs/AlAs Colloidal Quantum Dots

MOHAMMAD FARAJI, SAMIYE MATLOUB, AND HANNANEH DORTAJ

Quantum Photonics Research Laboratory (QPRL), Faculty of Electrical and Computer Engineering, University of Tabriz, Tabriz 5166614761, Iran

Corresponding author: Samiye Matloub (matloub@tabrizu.ac.ir)

ABSTRACT In the context of advancing photonics technologies, there is an increasing demand for broadband and ultrafast optical modulators to support next-generation telecommunication networks and ultrafast quantum information processing. Existing modulators are limited by their inability to efficiently handle multiple channels, leading to challenges in high-speed optical communication systems. We introduce a novel two-channel quantum dot all-optical modulator (QD-AOM) designed to simultaneously modulate telecommunication wavelengths of 1.32 μm and 1.55 μm by utilizing the interaction between two pump signals (683 nm and 866 nm) and two probe signals (1.32 μm and 1.55 μm). This innovative device leverages InAs/AlAs core/shell colloidal quantum dots, offering a scalable, cost-effective, and efficient solution for next-generation optical communication networks and ultrafast quantum information processing. Theoretical modeling was performed by solving the 3D Schrödinger equation, coupled rate and propagation equations to simulate the device's performance. The model accounts for carrier transfer processes and the interaction between channels through Fluorescence Resonance Energy Transfer (FRET). Simulations demonstrated that the QD-AOM achieved modulation depths of 65% and 62% for channels corresponding to 1.55 μm and 1.32 μm, respectively, with bandwidths of 26.3 GHz and 19.7 GHz. The device maintained high stability and efficiency at room temperature, with minimal variation in modulation depth across different temperatures, indicating its robustness for practical applications. Its broadband response, high modulation depth, and robust performance make it an ideal candidate for integration into future high-speed communication systems, signal processing, and other photonics-based applications.

INDEX TERMS All-optical modulator, colloidal quantum dots, high modulation depth.

I. INTRODUCTION

Optical modulation is essential in photonics technologies, with growing demand for broadband and ultrafast modulation in the age of artificial intelligence [1]. All-optical modulation stands out for its ability to operate at ultrafast speeds and offer a broadband response, making it highly promising for future optical communication networks, ultrafast quantum information processing, and photonic computing systems [2], [3].

High-speed signal processing and optical communication technologies crucially rely on devices known as AOMs, where light modulation is achieved through interactions with other light sources [4], [5], [6]. The promise of all-optical signal processing as a transformative technology for future high-bit rate modulation and transparent optical networks is underscored by its inherent ability to reduce implementation costs significantly and eliminate bottlenecks in ultrafast signal processing. Notably, this progress is accomplished without the need for costly optical-electrical-optical equipment [7], [8], [9]. Additionally, it offers low loss, compact size, a small footprint, and low driving power [2], [10].

At present, most commercial modulators are made from silicon (Si) [11], [12], bulk lithium niobate (LN) [13], and indium phosphide (InP) [14]. While modulators on these

The associate editor coordinating the review of this manuscript and approving it for publication was Yang Yue.

three platforms demonstrate impressive performance, none of them meet the necessary standards for the next generation of communication systems. Numerous innovative applications have been developed for actively controlling light using semiconductor QDs. In this area, colloidal QDs (CQDs), synthesized by the solution process method, paves the way for low-cost, easy-fabrication, and room-temperature processing of optical devices [15], [16].

Recently, significant progress has been made in acousto-optic modulators operating at telecommunication wavelengths [17]. Exploiting the unique optical properties of 2D materials, a graphene-clad microfiber acousto-optic modulator has been experimentally realized, achieving a modulation depth (MD) of 38% and a modulation frequency of 200 MHz, where the signal light at 1550 nm is controlled by light at 1064 nm [18]. 2D hybrid organic-inorganic perovskites (HOIPs) have generated significant interest in various optoelectronic fields. In this study, highly stable 2D (C6H5C2H4NH3)2PbI4 nanocrystals were successfully prepared using the liquid-phase exfoliation method. The ultrafast nonlinear saturable absorption characteristics of these nanocrystals were examined across the near-infrared (NIR) to mid-infrared (MIR) spectral ranges. Leveraging the unique nonlinear optical properties of the 2D HOIPs, a highly stable mode-locked Er3+-doped fiber laser (EDFL) with a pulse duration of approximately 531 fs and a signal-to-noise ratio (SNR) of about 90 dB was achieved around 1.5 μm. Additionally, a robust Q-switched Er3+-doped fluoride fiber laser (EDFFL) with a pulse duration of approximately 553 ns and an SNR of about 40 dB was experimentally demonstrated around 2.8 μm [19]. Furthermore, an AOM utilizing a spatial cross-phase modulation method based on MXene has been designed. Here, a strong control light ($\sim$40 Wcm$-$2) at 671 nm modulates a weaker signal light at 532 nm [20].

A thermo-optic effect-based experimental design of a niobium carbide (Nb2C) two-channel AOM supported by a Nb2C-PVA film was recently completed. The optical data from control light at wavelengths of 793 nm and 980 nm was effectively modulated to signal light at telecommunication wavelengths of 1.5 μm and 2.0 μm by this Nb2C AOM. Low speed and low MD were indicated by the system's achievement of an MD of 23.3% and a maximum modulation frequency of 5 kHz [21].

An all-optical modulation scheme based on free-carrier absorption has been demonstrated in a Ge-on-Si rib waveguide operating in the mid-infrared wavelength range of 2–3.2 μm. Using a pump-probe geometry, a 1.54 μm pulsed source has been used to modulate CW signals in this spectral range, achieving modulation depth of up to 60% with pulse energies in the picojoule range. The system demonstrated a free-carrier lifetime of approximately 18 ns, enabling modulation rates in the 60 MHz range, demonstrating the potential of Ge-on-Si platforms for high-speed and mid-infrared photonic applications [22].

Thin-film lithium niobate (TFLN) modulators have recently become a viable option for attaining ultra-high bandwidth with low driving voltages and a small footprint [23], [24], [25]. According to recent research, using TFLN produces a modulator with an extrapolated 3 dB bandwidth of 170 GHz and an observed roll-off of only 2 dB from low frequencies up to 100 GHz. The measured voltage-length product of this subterahertz device is 3.3 V cm. A different device exhibits a 3 dB electro-optic bandwidth of 84 GHz; however, it is tuned for a lower voltage-length product of 2.2 V cm. During testing, both devices were able to achieve data speeds of up to 240 Gb/s at 80 Gbaud using eight-level pulse-amplitude modulation (PAM-8). These findings suggest that modulators are a beautiful option for optical communication systems of the future [26].

In this paper, a new conception of a two-channel QD-AOM is introduced. The innovative device is conceived to be synthesized through the solution-processed InAs/AlAs QD core/shell structure, which provides higher absorption, high efficiency, low-cost fabricating, room-temperature processing, ease of large-area fabrication, and high tunability [27], [28]. Distinguishing itself from conventional approaches, our novel two-channel QD-AOM boasts a unique capability: adjustability to modulate selective wavelengths through the careful tuning of QDs' sizes. The introduced two-channel QD-AOM is tuned to absorb at two wavelengths of 683 nm and 866 nm, and two independent probe signals at wavelengths of 1.32 μm and 1.55 μm are applied to enable stimulated emission and generate a modulated signal at the output of the structure. Notably, this is the first case where two distinct wavelengths in the telecommunication windows are simultaneously modulated by the stimulated recombination phenomenon using two pump signals of different wavelengths. This study employs a slab waveguide incorporating quantum dots (QDs) of two distinct sizes to create modulation channels. The modulation occurs through the interaction of incident optical signals from the pump and probe. To simulate and numerically model the proposed two-channel QD-AOM, we have formulated rate and propagation coupling equations. These equations account for carrier transfer processes, light propagation within the waveguide, and their respective effects. Additionally, the interplay between the two channels, which constitutes a crucial phenomenon in this proposed modulator, is explicitly captured in the equations. This high-speed two-channel QD-AOM with a high MD can be utilized in several applications, including thermal imaging, signal processing, high-speed computing systems, night vision cameras, wavelength de-multiplexing (WDM), optical communication networks based on dense wavelength division multiplexing (DWDM) technology, and free-space communication [29].

The proposed contributions can be summarized as follows.

- First, A novel two-channel quantum dot all-optical modulator (QD-AOM) utilizing colloidal InAs/AlAs structures fabricated through solution process methods has been presented.

- Second, a unique approach has been introduced by applying pump signals with different wavelengths (683 nm and 866 nm) to two channels to modulate two distinct wavelengths within the telecommunication windows (1.32 μm and 1.55 μm).
- Third, a theoretical model is developed involving the solution of the 3D Schrödinger equation, coupled rate equations, and propagation equations to evaluate the performance of the proposed QD-AOM. This model captures the stimulated recombination phenomenon, which is crucial for the modulation process, enabling efficient light modulation at the specified wavelengths.
- Fourth, a comprehensive simulation is conducted to assess the overall performance of the device under various conditions, including different bit rates for each channel, and investigate the impact of carrier transfer between channels through Fluorescence Resonance Energy Transfer (FRET)?.
- Fifth, based on simulation results, in the pump power of 100 mW and probe power of -20 dBm, for the absorption of 866 nm (channel-1) and 683 nm (channel-2) and stimulated emission of 1.55 μm (channel-1) and 1.32 μm (channel-2), modulation depths of 65% and 62% and bandwidths of 26.3 GHz and 19.7 GHz are achieved for channels-1 and 2, respectively.
- Lastly, the fabrication feasibility and temperature variations on MD are explored. Our results indicate that the device, fabricated through a solution-processed method, exhibits significant stability at room temperature, with negligible changes in MD across different temperatures, demonstrating its robustness for practical applications.

II. THE PROPOSED TWO-CHANNEL QD-AOM

Our study presents a new and innovative approach utilizing two distinct sizes of core/shell (QDs) that can be synthesized through a solution process. This approach allows us to engineer a high-contrast, two-channel QD-AOM. The core is composed of InAs, while the shell is composed of AlAs, forming the absorber layer integral to the proposed structure.

Illustrated in Figure 1(a), two laser beams, each with different wavelengths, serve as both pump and probe signals, traversing separate channels. It would be helpful to note that the QDs can be distinguished based on their radii, with R_1 and R_2 representing channel-1 and channel-2, respectively. In the realm of experimental fabrication for diverse applications, including QD-SOAs, QD-lasers, and more [30], [31], [32], [33], [34], slab waveguides play a pivotal role. Traditionally, carrier injection via electrical pumping involves incorporating electron and hole transfer layers alongside the active layer and substrate. However, our approach diverges by utilizing colloidal QDs exclusively within the active layer. Notably, we exclude transmission layers in favor of utilizing an optical pump for carrier population inversion.

Interband transitions between quantized energy levels within the valence band and the conduction band play a crucial role in modulation processes. In our proposed structure, a Gaussian pulse serves as the information pump signal, operating at wavelengths of 866 nm (683 nm), corresponding to channel-1 (channel-2). Simultaneously, a continuous wave (CW) is applied as the probe signal, operating at a wavelength of 1.55 μm (1.32 μm). The structural parameters are tailored for QD radii, with R_1 (R_2) set to 3.75 nm (3 nm). It is important to note that utilizing QDs of sizes other than the specified values in the proposed structure will require lasers of varying wavelengths, following the principles of quantum mechanics and the permissible energy levels for electron presence. Upon applying the pump signal, electrons undergo absorption from the excited state of the valence band (ES^v) to the excited state of the conduction band (ES^c). Subsequently, these excited electrons rapidly transition to the ground state of the conduction band (GS^c) due to a relatively short relaxation time. Simultaneously, the CW probe signal induces stimulated emission, which causes electrons to transition from GS^c to the ground state of the valence band (GS^v) and generate coherent photons. This phenomenon results from population inversion within the conduction band. The carriers involved in the stimulated emission process have a significant influence on the performance of the modulator. To investigate this effect and the changes in these carriers, we have introduced a parameter called Probe Gain (PG). By using this parameter, we have characterized the behavior of these carriers. In the absence of the pump signal, no signal is received at the output. The PG spectrum, illustrating the relationship between incident light energy and the PG produced by stimulated emission, is visually represented in Figure 1(b). This depiction provides insights into the performance characteristics of our proposed system, showcasing its efficacy in achieving signal modulation.

In the quest for optimal performance in the two-channel QD-AOM, a departure from continuous pump signals is undertaken by applying a pulse train. This pulse train, which periodically switches off the pump at a predetermined repetition rate, introduces a dynamic modulation aspect to the process. To generate an inverted Gaussian pulse train, an inverter or NOT gate can be employed [35], [36]. Following this, a CW is introduced as the probe signal. In the presence of the pulse train pump signal—effectively inducing carrier population inversion—the output at the two-channel QD-AOM reveals a modulated probe signal. The strategic turning off of the pump signal disrupts the population inversion between GS^c and GS^v, resulting in a reduction of the output probe signal. By employing On-Off keying with the pump signal wavelength set at 866 nm, the probe signal at 1.55 μm faithfully mirrors the pump alterations, culminating in a modulated signal. In the pursuit of compact and high-performance devices in optoelectronics, we extend

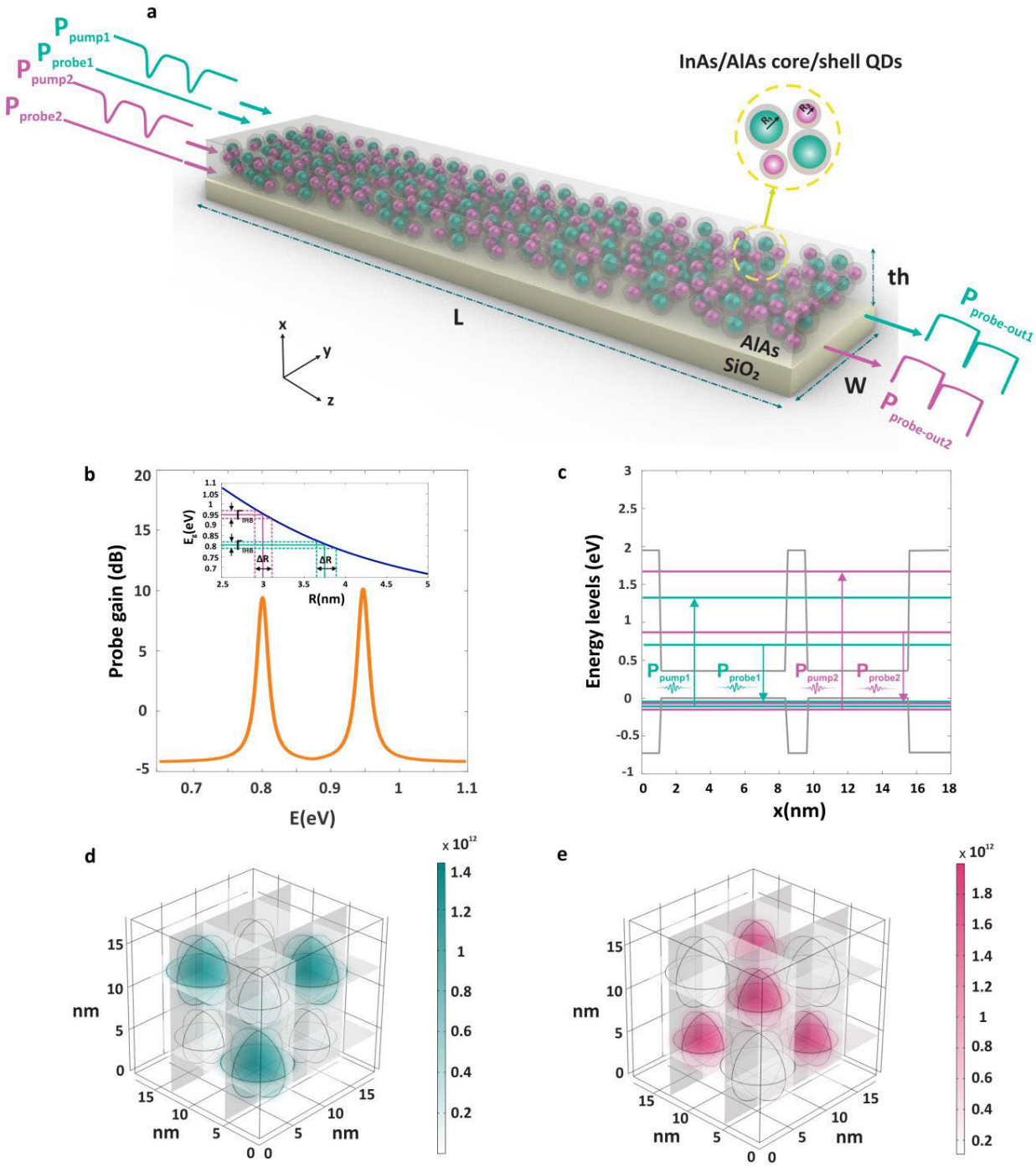

FIGURE 1. The schematic view of the designed QD-AOM. (a) The schematic of the proposed structure contains an array of two different sizes of InAs/AlAs core/shell QDs. (b) The PG spectrum versus the energy of the incident light. The diagram of bandgap energy as a function of radiuses of QDs is depicted and inserted in this figure. (c) The simulated energy band structure of the proposed device by the absorption and stimulated recombination mechanism. The 3D display of wave functions simulated by FEM software has been illustrated for (d) channel-1 and (e) channel-2.

the utility of the structure to modulate a probe signal at 1.32 μm in the pump signal wavelength of 683 nm. To achieve this, we incorporate another size of QDs, optimizing the structure's functionality and broadening its application for modulation at two distinct wavelengths. This strategic utilization of different QD sizes enhances the versatility and adaptability of the proposed system.

III. THEORETICAL MODELING OF THE PROPOSED TWO-CHANNEL QD-AOM IN THE RATE EQUATION FRAMEWORKOUR STUDY PRESENTS A NEW AND INNOVATIVE APPROACH UTILIZING TWO DISTINCT SIZES OF CORE/SHELL

In this section, we delve into the theoretical underpinnings of the proposed two-channel QD-AOM. The modal analysis

TABLE 1. Material properties used in calculating the 3D schrodinger equation [38], [39], [40], [41].

Description	Symbol	Materials	
		InAs	AlAs
Electron affinity	χ [eV]	4.9	3.3
Bandgap Energy	E_g [eV]	0.36	2.67
Effective mass of the electron	m_{e^*}	$0.023m_0$	$0.14m_0$
Effective mass of the hole	m_{h^*}	$0.41m_0$	$0.8m_0$

begins with the solution of the 3D Schrödinger equation, which leads to the determination of eigen-energies, wavefunctions, and the energy band diagram. This comprehensive approach lays the foundation for a detailed understanding of the structure's quantum mechanical aspects. Following the modal analysis, we evaluate the performance of the two-channel QD-AOM. The coupled rate and propagation equations are systematically solved to characterize the essential metrics governing the modulator's behavior. Moreover, our theoretical framework incorporates the nuanced effects of homogeneous broadening (HB) and inhomogeneous broadening (IHB), as well as the impact of FRET, which collectively influence the coupled rate equations. This inclusive modeling approach allows for a holistic exploration of the device's dynamics, offering insights into its operational characteristics and potential improvements.

A. THE MODAL ANALYSIS OF THE TWO-CHANNEL QD-AOM

Utilizing the effective mass approximation method and solving the 3D Schrödinger equation with the values specified in Table 1, the energy band diagram of the structure has been obtained, consistent with our prior work [37]. Furthermore, the absorption and stimulated emission processes have been demonstrated in Figure 1 (c). Also, the computed wavefunctions corresponding to the GS^c for channel-1 and channel-2 have been obtained using the Finite Element Method (FEM) software and illustrated in Figure 1 (d, e), respectively. To simulate the device realistically, a periodic boundary condition is applied, extending the simulated device to match practical system conditions.

Due to the constraints imposed by synthesis conditions in the solution process method, achieving the precisely designed size of QDs cannot be realized [29], [42], [43], [44]. Therefore, the non-uniformity in QD size has an influential impact on the absorption spectra; this process is known as inhomogeneous broadening (IHB). To address this inherent variability, a sophisticated modeling approach is adopted, wherein the distribution of energy states is methodically characterized by a Gaussian profile. It would be helpful to mention that the Gaussian profile can act as an indicator of any potential deviations in the size of the synthesized QDs from their expected radius. This modeling framework necessitates the partitioning of the QDs ensemble into 2M + 1 groups, each comprised of uniform QDs. This categorization is achieved with an energy spacing of $\Delta E = 1$ meV [45], [46], [47], [48], [49]. This meticulous strategy ensures a comprehensive representation of the diverse QD sizes, enhancing the accuracy and reliability of our theoretical framework. The Gaussian distribution (G_i) can be accurately represented by the following equation:

$$E^p_{n,i} = E^p_{0,i} - (M + 1 - n) \times \Delta E \; n = 1, \ldots, 2M+1 \; i = 1, 2 \; p = \text{pump, probe} \tag{1}$$

$$G_i(E^p_{n,i}) = \frac{1}{\sqrt{2\pi}\xi_0} \exp\left[\frac{-\left(E^p_{n,i} - E^p_{0,i}\right)^2}{2\xi_0^2}\right] \tag{2}$$

The modeling framework $E^p_{0,i}$ signifies the transfer energy of the most probable size within the QDs ensemble (M+1-th QD group). The index i is fixed at 1 for channel-1 and 2 for channel-2, the index p is related to the pump's and probe's incident lights, suggesting that these equations need to be written independently for each, and the n corresponds to the index denoting the number of active modes. Additionally, ξ_0 denotes the QD coverage and is defined as $\xi_0 = (1/2.35)\Gamma_{IHB}$, where $\Gamma_{IHB} = 20$meV is the full width of half maximum (FWHM) of the Gaussian profile [29], [45]. Observations derived from Figure 1(b), based on simulation results, reveal alterations in QD sizes from the two central radii (3 nm and 3.75 nm) by ΔR, corresponding to an energy difference of Γ_{IHB}. Consequently, due to the inhomogeneous broadening of the QD radius, it is predicted that the overlap of the PG spectrum will not be detectable according to the considered value for Γ_{IHB} if the experimental device is built for the proposed structure. Furthermore, intrinsic factors, such as pressure or temperature, induce interactions between carrier-carrier and phonon-carrier, homogeneously affecting all groups. This results in the manifestation of homogeneous broadening (HB) on the energy levels, modeled by a Lorentzian profile with $\Gamma_{HB} = 20$ meV as its FWHM at room temperature [37], [50].

$$B_{m,n}(E^p_{n,i} - E^p_{m,i}) = \frac{1}{\pi} \frac{\Gamma_{HB}/2}{\left(E^p_{n,i} - E^p_{m,i}\right)^2 + (\Gamma_{HB}/2)^2} \quad n = 1, \ldots, 2M + 1, \quad m = \text{number of photon modes} \tag{3}$$

The HB for the mth photon mode (and nth QD group active mode) is represented by the symbols $B_{m,n}$. Considering the acquired broadenings, the linear interband absorption coefficient from ES^v to ES^c, resulting from the applied pump power, is obtained by [51]:

$$\alpha^{Pump}_{m,n,i} = \frac{2}{V_{QD,i}} \frac{e^2}{c\varepsilon_0 n_i^{pump}} \frac{E^{pump}_{n,i}}{\hbar} | < \Psi^v_{e,i} | \widehat{e.r} | \Psi^c_{e,i} > |^2 \times G_i(E^{pump}_{n,i}) B_{m,n}(E^{pump}_{n,i} - E^{pump}_{m,i}) \tag{4}$$

In these equations, c represents the free space light speed, ε_0 is the free space permittivity, n_i^{pump} is the refractive index related to pump wavelengths, $\hbar$ is the reduced Planck's constant, e is the electron charge, and $V_{QD,i}$ is the volume of the QD of the corresponding channel. The term $|< \Psi^v_{e,i}|\widehat{e}.\widehat{r}|\Psi^c_{e,i} >|$ signifies the interband transition dipole moment. Ultimately, total interband absorption is achieved through:

$$\alpha^T_{m,i}(t) = \int_0^L [\sum_{n=1}^{2M+1} \alpha^{pump}_{m,n,i}(f^v_{e_{n,i}}(z,t) - f^c_{e_{n,i}}(z,t))]dz \quad (5)$$

where L is the waveguide length. Similarly, the PG resulting from stimulated emission transitioning from GS^c to GS^v by applying probe power is determined by:

$$g^{probe}_{m,n,i} = \frac{2}{V_{QD,i}} \frac{e^2}{cn_i^{probe}\hbar\varepsilon_0} E^{probe}_{n,i} |< \Psi^c_{g,i}|\widehat{e}.\widehat{r}|\Psi^v_{g,i} >|^2 \times G_i(E^{probe}_{n,i}) B_{m,n}(E^{probe}_{n,i} - E^{probe}_{m,i}) \quad (6)$$

In this context, n_i^{probe} represents the refractive index related to probe wavelengths, and the term $|< \Psi^c_{g,i}|\widehat{e}.\widehat{r}|\Psi^v_{g,i} >|$ signifies the interband transition dipole moment. In final, the total PG is obtained through the following:

$$g^T_{m,i}(t) = \int_0^L [\sum_{n=1}^{2M+1} g^{probe}_{m,n,i}(f^c_{g_{n,i}}(z,t) - f^v_{g_{n,i}}(z,t))]dz \quad (7)$$

On the other hand, FRET is a non-radiative energy transfer process in which a donor (a QD with a smaller radius) transfers the energy to an acceptor (a QD with a larger radius) through dipole-dipole interactions [52]. The transfer rate depends on the distance between two QDs and the spectral overlap. In the proposed two-channel QD-AOM, utilizing two distinct groups of QDs, this transfer process is considered a transmission rate ($W^l_{12,n}$) attained through:

$$W^l_{12,n,i} = \frac{2}{V_{eff}} \frac{e^2}{\hbar(n_i^p)^2\varepsilon_0} E^l_{12,n} |< \Psi^c_{l,1}|\widehat{e}.\widehat{r}|\Psi^c_{l,2} >|^2 \times B_{m,n}(E^l_{12,m} - E^l_{12,n}) G(E^l_{12,n}) \quad l = GS^c, ES^c \quad (8)$$

Here V_{eff} represents the effective volume of QDs with different sizes, and $E^l_{12} = E^l_1 - E^l_2$, which E^l_1 is the energy associated with the specific level in channel-1 and E^l_2 is the energy related to the same level in channel-2. The time constants related to transfer between two different sizes of QDs are calculated by $\tau^l_{up(down)\_trans} = 1/W^l_{12,n}$ and involved in coupled rate equations.

B. THE RATE AND PROPAGATION EQUATIONS

The operational efficiency of the devised two-channel QD-AOM is predominantly governed by the dynamics of carriers and photons. While the semiconductor Bloch equation offers a more precise method for analyzing and modeling these characteristics, its computational complexity and time-consuming nature prompted the utilization of rate and propagation equations, which have yielded satisfactory results. The propagation of square-pulse train pump and CW probe signals is carried out along the z-direction. The advanced coupled rate and propagation equations for the proposed structure, employing the parameters outlined in Table 2, are expressed as (9)–(16), as shown at the top of next page. Where $n^c_{g_{n,i}}$, $n^c_{e_{n,i}}$, $n^v_{g_{n,i}}$, and $n^v_{e_{n,i}}$ represent the number of electrons in GS^c, ES^c, GS^v, and ES^v, respectively in channel-1 and channel-2. Additionally, $P^{pump}_{m,i}$ and $P^{probe}_{m,i}$ denote the optical pump power and the CW probe power, respectively. The corresponding carrier occupation probabilities are denoted as $f^c_{g_{n,i}}$, $f^c_{e_{n,i}}$, $f^v_{g_{n,i}}$, and $f^v_{e_{n,i}}$ in GS^c, ES^c, GS^v, and ES^v, respectively. Γ is the waveguide's optical confinement factor. Besides, the number of electrons associated with their corresponding occupation probabilities is calculated by $n^{c(v)}_{g_{n,i}}(z,t) = f^{c(v)}_{g_{n,i}}(z,t)N^{c(v)}_{G_i}$, $n^{c(v)}_{e_{n,i}}(z,t) = f^{c(v)}_{e_{n,i}}(z,t)N^{c(v)}_{E_i}$. The time constants corresponding to these carrier transition processes are named τ^v_{ge} (electron decay time from the GS^v to the ES^v), τ^c_{eg} (electron decay time from the ES^c to the GS^c), τ_{gr} (carrier lifetime from the GS^c to the GS^v), τ_{er} (carrier lifetime from the ES^c to the ES^v). The time constants according to the FRET mechanism are illustrated as $\tau_{down-trans-g(e)}$(electron transition time from the GS^c (ES^c) of channel-1 to the GS^c (ES^c) of channel-2) and $\tau_{up-trans-g(e)}$(electron transition time from the GS^c (ES^c) of channel-2 to the GS^c (ES^c) of channel-1). The time constants associated with the electron escape process in the valence and conduction bands are determined as follows:

$$\tau^{c(v)}_{ge} = \tau^{c(v)}_{eg} \frac{D^{c(v)}_g}{D^{c(v)}_e} \exp(\Delta E^{c(v)}_{eg}/KT) \quad (17)$$

K is the Boltzmann constant, and T is the temperature (Kelvin scale). $\Delta E^{c(v)}_{eg}$ is the energy interval between ES$^{c(v)}$ and GS$^{c(v)}$ [53], [54], [55]. Degeneracies are determined by $D^c_g = 1, D^c_e = 3, D^v_g = 1$, and $D^v_e = 3$ in GS^c, ES^c, GS^v, and ES^v, respectively. The total number of electrons in each state, GS^c, ES^c, GS^v, and ES^v, is represented by $N^{c(v)}_{G_i} = N_{QD,i}V_d D^{c(v)}_g$, $N^{c(v)}_{E_i} = N_{QD,i}V_d D^{c(v)}_e$, respectively. Here, $N_{QD,i}$ is the density of QDs, and V_d is the volume of the active region for both channels.

C. SIMULATION RESULTS AND DISCUSSION

In this section, the performance of the proposed two-channel QD-AOM is evaluated by solving the advanced coupled rate and propagation equations (9)–(16), considering the parameters referred to in Table 2. The method used to solve the coupled equations involved dividing the length of the proposed structure into 100 equal regions in the z-direction, which the probe and the pump signals propagated in. In addition, the time domain was partitioned into smaller intervals to analyze the structural features during each step. The solution approach used is similar to the work done by Kim et al. [48], which is experimental and theoretical research.

The most critical metrics for assessing the characteristics of a two-channel QD-AOM are the frequency response and MD. Furthermore, the transfer of carriers between two

different sizes of QDs in two channels is investigated in all simulations.

In Figure 2, the overall performance of the proposed device is investigated with a pump power of 100 mW and a pulse train frequency of 1 GHz in three modes. The input probe power is set at −20 dBm to operate in the linear region. Firstly, a Gaussian pulse train as a pump signal has been applied to channel-1, and a constant CW pump signal

$$\frac{dn^c_{g_{n,1}}(z,t)}{dt} = -\frac{n^c_{g_{n,1}}(z,t)}{\tau_{down\_trans\_g}}(1-f^c_{g_{n.2}}(z,t)) + \frac{n^c_{g_{n,2}}(z,t)}{\tau_{up\_trans\_g}}(1-f^c_{g_{n,1}}(z,t)) + \frac{n^c_{e_{n,1}}(z,t)}{\tau^c_{eg}}(1-f^c_{g_{n,1}}(z,t)) - \frac{n^c_{g_{n,1}}(z,t)}{\tau^c_{ge}}(1-f^c_{e_{n,1}}(z,t)) - \frac{n^c_{g_{n,1}}(z,t)}{\tau_{gr}}(1-f^v_{g_{n,1}}(z,t)) - \sum_{m=1}^{2M+1}\Gamma Lg_{m,n,1}\frac{P^{probe}_{m,1}(z,t)}{E^{probe}_{m,1}}(f^c_{g_{m,1}}(z,t)-f^v_{g_{m,1}}(z,t)) \tag{9}$$

$$\frac{dn^c_{g_{n,2}}(z,t)}{dt} = \frac{n^c_{g_{n,1}}(z,t)}{\tau_{down\_trans\_g}}(1-f^c_{g_{n.2}}(z,t)) - \frac{n^c_{g_{n,2}}(z,t)}{\tau_{up\_trans\_g}}(1-f^c_{g_{n,1}}(z,t)) + \frac{n^c_{e_{n,2}}(z,t)}{\tau^c_{eg}}(1-f^c_{g_{n.2}}(z,t)) - \frac{n^c_{g_{n,2}}(z,t)}{\tau^c_{ge}}(1-f^c_{e_{n.2}}(z,t)) - \frac{n^c_{g_{n.2}}(z,t)}{\tau_{gr}}(1-f^v_{g_{n.2}}(z,t)) - \sum_{m=1}^{2M+1}\Gamma Lg_{m,n,2}\frac{P^{probe}_{m,2}(z,t)}{E^{probe}_{m,2}}(f^c_{g_{m,2}}(z,t)-f^v_{g_{m,2}}(z,t)) \tag{10}$$

$$\frac{dn^c_{e_{n,1}}(z,t)}{dt} = -\frac{n^c_{e_{n,1}}(z,t)}{\tau_{down\_trans\_e}}(1-f^c_{e_{n.2}}(z,t)) + \frac{n^c_{e_{n,2}}(z,t)}{\tau_{up\_trans\_e}}(1-f^c_{e_{n,1}}(z,t)) \times \frac{n^c_{g_{n,1}}(z,t)}{\tau^c_{ge}}(1-f^c_{e_{n,1}}(z,t)) - \frac{n^c_{e_{n,1}}(z,t)}{\tau^c_{eg}}(1-f^c_{g_{n,1}}(z,t)) - \frac{n^c_{e_{n,1}}(z,t)}{\tau_{er}}(1-f^v_{e_{n,1}}(z,t)) + \sum_{m=1}^{2M+1}\Gamma L\alpha_{m,n,1}\frac{P^{pump}_{m,1}(z,t)}{E^{pump}_{m,1}}(f^v_{e_{m,1}}(z,t)-f^c_{e_{m,1}}(z,t)) \tag{11}$$

$$\frac{dn^c_{e_{n,2}}(z,t)}{dt} = \frac{n^c_{e_{n,1}}(z,t)}{\tau_{down\_trans\_g}}(1-f^c_{e_{n.2}}(z,t)) - \frac{n^c_{e_{n,2}}(z,t)}{\tau_{up\_trans\_g}}(1-f^c_{e_{n,1}}(z,t)) \times \frac{n^c_{g_{n,2}}(z,t)}{\tau^c_{ge}}(1-f^c_{e_{n,2}}(z,t)) - \frac{n^c_{e_{n,2}}(z,t)}{\tau^c_{eg}}(1-f^c_{g_{n,2}}(z,t)) - \frac{n^c_{e_{n,2}}(z,t)}{\tau_{er}}(1-f^v_{e_{n,2}}(z,t)) + \sum_{m=1}^{2M+1}\Gamma L\alpha_{m,n,2}\frac{P^{pump}_{m,2}(z,t)}{E^{pump}_{m,2}}(f^v_{e_{m,2}}(z,t)-f^c_{e_{m,2}}(z,t)) \tag{12}$$

$$\frac{dn^v_{g_{n,i}}(z,t)}{dt} = \frac{n^c_{g_{n.i}}(z,t)}{\tau_{gr}}(1-f^v_{g_{n.i}}) + \frac{n^v_{e_{n,i}}(z,t)}{\tau^v_{eg}}(1-f^v_{g_{n.i}}(z,t)) - \frac{n^v_{g_{n,i}}(z,t)}{\tau^v_{ge}}(1-f^v_{e_{n.i}}(z,t)) + \sum_{m=1}^{2M+1}\Gamma Lg_{m,n,i}\frac{P^{probe}_{m,i}(z,t)}{E^{probe}_{m,i}}(f^c_{g_{m,i}}(z,t)-f^v_{g_{m,i}}(z,t)) \tag{13}$$

$$\frac{dn^v_{e_{n,i}}(z,t)}{dt} = \frac{n^c_{e_{n.i}}(z,t)}{\tau_{er}}(1-f^v_{e_{n.i}}(z,t)) + \frac{n^v_{g_{n,i}}(z,t)}{\tau^v_{ge}}(1-f^v_{e_{n.i}}(z,t)) - \frac{n^v_{e_{n,i}}(z,t)}{\tau^v_{eg}}(1-f^v_{g_{n.i}}(z,t)) - \sum_{m=1}^{2M+1}\Gamma L\alpha_{m,n,i}\frac{P^{pump}_{m,1}(z,t)}{E^{pump}_{m,1}}(f^v_{e_{m,1}}(z,t)-f^c_{e_{m,1}}(z,t)) \tag{14}$$

$$\frac{\partial P^{pump}_{m,i}(z,t)}{\partial z} = (-\sum_{n=1}^{2M+1}\Gamma\alpha_{m,n,i}(f^v_{e_{n,i}}(z,t)-f^c_{e_{n,i}}(z,t))-\alpha_{int})P^{pump}_{m,i}(z,t) \tag{15}$$

$$\frac{\partial P^{probe}_{m,i}(z,t)}{\partial z} = (\sum_{n=1}^{2M+1}\Gamma g_{m,n,i}(f^c_{g_{n,i}}(z,t)-f^v_{g_{n,i}}(z,t))-\alpha_{int})P^{probe}_{m,i}(z,t) \tag{16}$$

TABLE 2. The parameters required in calculating rate and propagation equations [48], [56], [57], [58].

Parameters	Channel-1	Channel-2
Radius of QD [nm]	R_1=3.75	R_2=3
L [μm]	2000	
W [μm]	400	
th [μm]	20	
QD volume density (N_{QD}) [cm^{-3}]	2×10^{17}	2.3×10^{17}
The optical confinement factor (Γ)	0.11	
Refractive index	Pump:3.5709	Pump: 3.8670
	Probe: 3.4529	Probe: 3.4546
The intrinsic loss of the waveguide (α_{int}) [m^{-1}]	500	
The electron relaxation time from the ES^c to the GS^c (τ_{eg^c}) [ps]	1	
The electron relaxation time from the GS^v to the ES^v (τ_{ge^v}) [ps]	1	
The electron recombination time from the ES^c to the ES^v (τ_{er}) [ns]	0.4	
The electron recombination time from the GS^c to the GS^v (τ_{gr}) [ns]	0.4	

is applied to channel-2. In this mode, the output modulated probe signal for channel-1, and channel-2, as well as the PG for both channels, are calculated and depicted in Figure 2 (a, d, g), respectively. Secondly, a constant CW pump signal has been applied to channel-1, and a Gaussian pulse train pump signal has been applied to channel-2. In this mode, the output modulated probe signal for channel-1 and channel-2 and the PG for both channels are calculated and depicted in Figure 2 (b, e, h), respectively. Thirdly, Gaussian pulse trains as pump signals have been applied to both channels. In this mode, the output modulated probe signal for channel-1 and channel-2 and the PG for both channels are calculated and depicted in Figure 2 (c, f, i), respectively. According to these figures, when the Gaussian pulse train is periodically applied to switch off the pump signal in just one channel to modulate the input probe signal, the other channel is also affected. In other words, due to the carrier transfer between two channels (the FRET process), the other channel is modulated to negligible, and the PG profile is altered for both channels.

According to Figure 2 (g, h, i), the carrier recovery time is approximately < 0.5 ns, indicative of a subsequent frequency response anticipated to be within the range of a few GHz for this device. A crucial determinant influencing the carrier recovery time is the relaxation time of the carriers. Given its picosecond scale, this time parameter does not pose a limiting factor for the operational frequency of the device. Another determinant contributing to the limitation of the carrier recovery time in the proposed structure is the FWHM of the Gaussian pulse width of the input optical pump. Consequently, an additional crucial parameter deserving consideration in the device's output is the MD. In instances of population inversion, a faster turn-off of the optical pump (characterized by a smaller pulse width) occurs due to insufficient input probe power, which promptly releases carriers from the conduction band.

Consequently, the input probe struggles to promptly follow the optical pump, leading to a diminished MD in the output probe signal. It is noteworthy that the gain recovery time, which operates on a nanosecond scale, does not significantly contribute to the swift release of carriers from the conduction band. Therefore, to achieve an acceptable MD at the device's output, a deliberate increase in the pulse width of the optical pump is necessitated. This increase concurrently elongates the carrier recovery time and consequently diminishes the bandwidth.

A noteworthy conclusion regarding Figure 2 is that the two channels operate independently in the modulation process, except for the FRET process, which was explained earlier. Additionally, the data suggests that the two channels need not operate at the same bit rate and can have different bit rates. In general, the purpose of Figure 2 is to evaluate the performance of the proposed structure under challenging conditions, especially when two channels have the same bit rate. Simulations have been performed to measure their influence on each other and to assess their flexibility.

Electron occupation probabilities as a function of incident light energy for GS^c, ES^c, GS^v, and ES^v are demonstrated in Figure 3 (a, b, c, d), respectively. Notably, the peaks in these probabilities align with the wavelengths of the incident lights. Similarly, Figure 3 (e, f, g, h) depicts electron occupation probabilities as a function of time for GS^c, GS^v, ES^c, and ES^v, respectively. In all instances of Figure 3 (a, b, c, d), the probabilities are calculated at both the beginning and end of the structure. The results indicate that electron occupation probabilities in the conduction band are higher at the commencement of the structure compared to those at the end, owing to the incident light being applied at the input facet of the waveguide.Consequently, the absorption processes occurring along the waveguide lead to a reduction in the number of photons, resulting in diminished interband transitions and, subsequently, a decrease in electron occupation probabilities at the output facet.

Analyzing the time responses reveals that, before periodically switching off the pump signal, a population inversion occurs between the energy levels of the conduction and valence bands. Upon the Gaussian pump signal being applied, the absorption process decreases, and carriers in the conduction band are reduced through the probe signal (stimulated emission). At this time, the carriers of the valance band increase, leading to a decrease in the output probe signal. Subsequently, by switching on the pump signal, the output probe signal increases, eventually manifesting a modulated probe signal that mirrors the changes in the pump signal at the output facet of the waveguide.

The PG, depicted as a function of output probe power for channel-1 and channel-2 is illustrated in Figure 4 (a, d), respectively. Notably, this depiction signifies the selection of the linear region for the modulation process. Furthermore, the PG is calculated for three specific pump power levels,

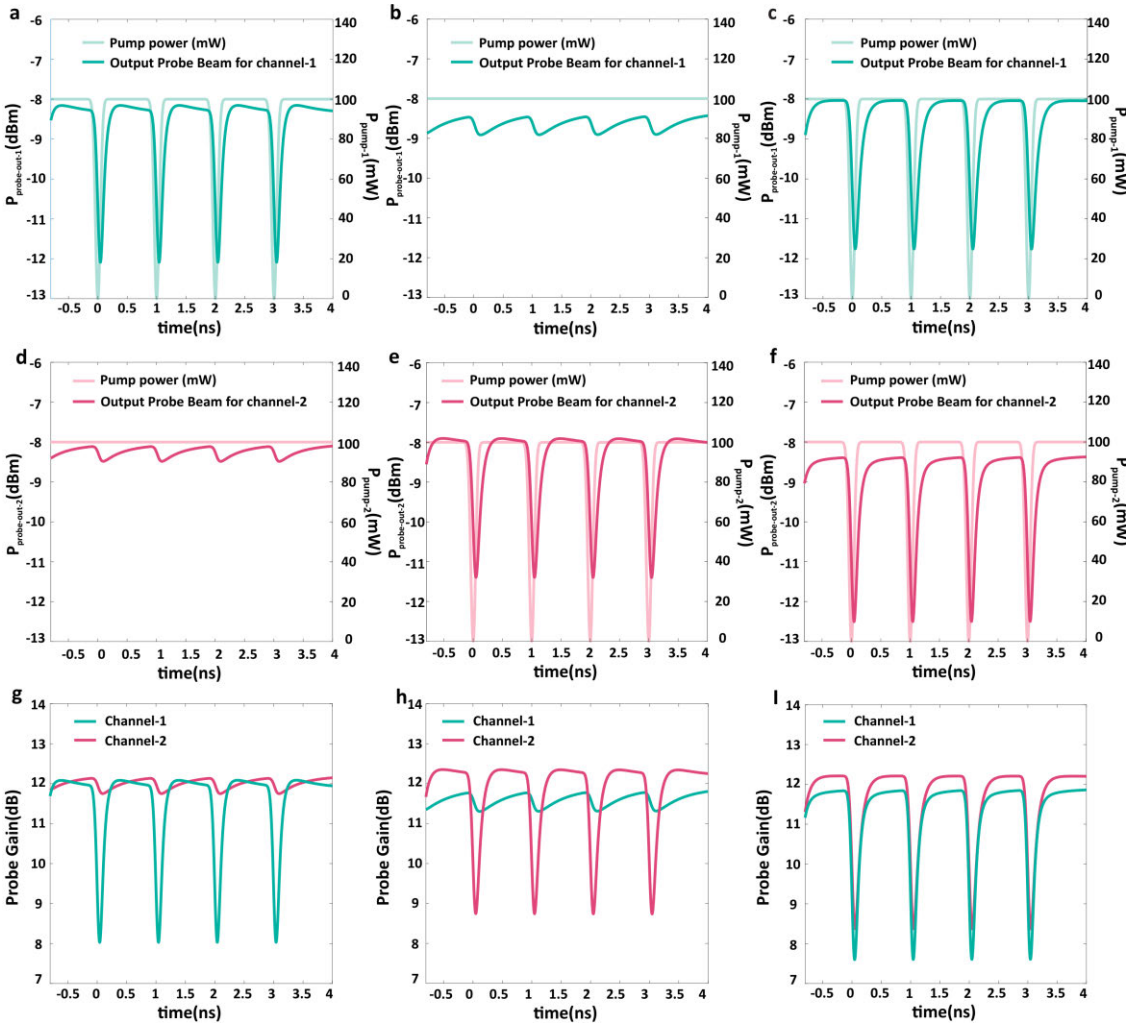

FIGURE 2. The general performance of two-channel QD-AOM with the pump power of 100 mW, the input power of −20 dBm, and the pulse train frequency of 1GHz. Output probe beam for channel-1 (a) when a Gaussian pump signal has been applied to channel-1 and a CW pump signal has been applied to channel-2, (b) when a CW pump signal has been applied to channel-1 and a Gaussian pump signal has been applied to channel-2, and (c) when Gaussian pump signals have been applied to both channels. Output probe beam for channel-2 (d) when a Gaussian pump signal has been applied to channel-1 and a CW pump signal has been applied to channel-2, (e) when a CW pump signal has been applied to channel-1 and a Gaussian pump signal has been applied to channel-2, and (f) when Gaussian pump signals have been applied to both channels. The time-resolved PG for channel-1&2 (g) when a Gaussian pump signal has been applied to channel-1 and a CW pump signal has been applied to channel-2, (h) when a CW pump signal has been applied to channel-1 and a Gaussian pump signal has been applied to channel-2, and (i) when Gaussian pump signals have been applied to both channels.

revealing an increase in the linear region as the pump power is augmented. Figure 4 (b, e) illustrates the output probe power as a function of the input probe power for channel-1 and channel-2, respectively. It is discernible that with an increase in input probe power, the output probe power linearly increases until reaching saturation points of −7.2 dBm and −6.7 dBm for channel-1 and channel-2, respectively, at an input pump power of 100 mW.

Given the absence of the absorption process during the applied of a Gaussian pulse, the PG diminishes, with a more pronounced decrease at higher input probe powers. Therefore, the output probe power approaches zero with increasing input probe power. Consequently, the MD, defined as the difference between the maximum and minimum values of the output probe power, increases. Subsequently, a further increase in input probe power leads to the occurrence of the absorption process instead of the PG. This results in an attenuation of the output probe power, diminishing the maximum level and, consequently, reducing the MD. These dynamics are visualized in Figure 4 (c, f), depicting the MD as a function of the input probe power for channel-1 and channel-2, respectively. Based on the data presented in Figure 4 (g, h), it becomes evident that the frequency response or bandwidth of the structure is inversely proportional to the input probe power. This trend is observed in both channels, indicating that the effect is independent of the specific channel used.

In Figure 4 (i), the bandwidth of the structure is plotted against the changes in input probe powers for both channels. It is worth noting that channel-1 exhibits a relatively larger bandwidth than channel-2 at low probe powers. At a probe

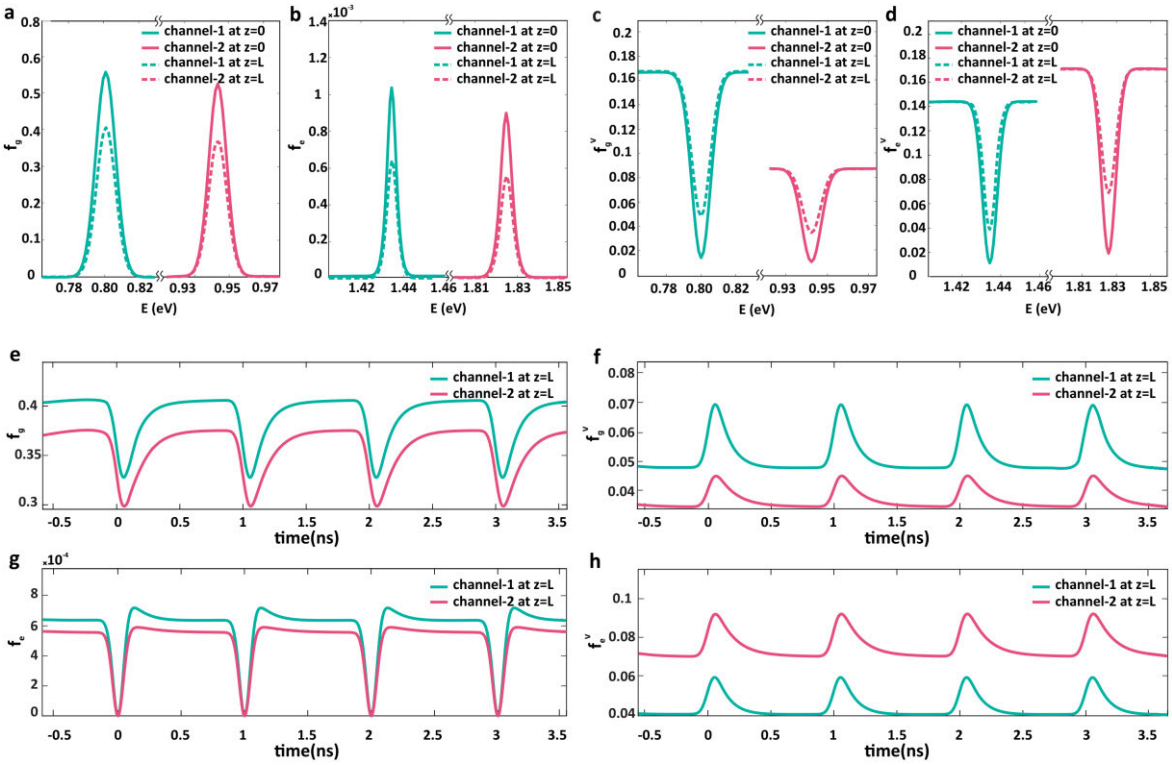

FIGURE 3. Electron occupation probabilities as a function of incident light energy in z=0 and z=L for both channels, (a) for GS^c (b) for ES^c, (c) for GS^v, and (d) for ES^v. Electron occupation probabilities as a function of time in z=L for both channels, (e) for GS^c, (f) for GS^v, (g) for ES^c, and (h) for ES^v.

power of −40 dBm, the bandwidth for channel-1 is 105 GHz, while that for channel-2 is 58 GHz. The data demonstrates that as the input probe power is increased, the bandwidth values for both channels remain at a reasonable and appropriate level. Specifically, when the probe power is set to −20 dBm, channel-1 and 2 achieved impressive bandwidths of 26.3 GHz and 19.7 GHz, respectively

The frequency responses, as depicted in Figure 5 (a, d), reveal that an increase in pump power leads to a wider bandwidth for the device. The PG for channel-1 and channel-2 as a function of pump power are presented in Figure 5 (b, e), indicating a decrease in the PG with an increase in input probe power. Furthermore, with an increase in input pump power at a fixed probe power of −20 dBm, we anticipate that the PG will rise due to enhanced carrier absorption from the valence band to the conduction band. This results in an increase in excited carriers in the conduction band. The heightened carriers in ES^c lead to an increase in stimulated recombination in the presence of the probe power, consequently elevating the PG.

Furthermore, by increasing the pump power, the PG increases until the ES^c is not saturated with excited carriers. As observed in Figure 5 (b, e), the PG changes almost linearly with the increase in pump power up to approximately 50 mW. Beyond this point, the changes in the output PG become minimal, indicating the saturation of ES^c. Consequently, the PG stabilizes at high pump power. Figure 5 (c, f) illustrates that an increase in input probe power corresponds to an increase in MD. As the input probe power rises, the stimulated recombination rate increases. Additionally, applying a Gaussian pulse to turn off the pump power leads to a rapid reduction in the density of electrons in the conduction band. Consequently, the minimum level of the output probe power decreases, leading to an increase in MD.

The carrier lifetime stands as a critical parameter influencing the PG of the device, and its determination is intricately linked to the conditions of the QD's fabrication process. Due to the presence of traps that modify the recombination process time, it is possible to control the recombination time by engineering the fabrication of these QDs. In Figure 6, the repercussions of alterations in carrier lifetime are explored in the context of frequency responses, and it is important to note that all simulations in this figure were conducted using the input pump power of 100 mW and the input probe power of −20 dBm for both channels. Figure 6 (a, b) demonstrates that an increase in carrier lifetime leads to a reduction in the bandwidth of the proposed device for both channels. As explicitly illustrated in Figure 6 (c), it is evident that even with a high lifetime, channel-1 and 2 have a bandwidth of 5 GHz and 12 GHz, respectively, in 1 ns.

Additionally, Figure 6 (d) delves into the effects of varying carrier lifetimes on MD. The results indicate that an increase in carrier lifetime corresponds to a decrease in MD. This phenomenon arises due to the extended lifetime, which leads to a diminished probability of spontaneous recombination of electrons. Consequently, the noise stemming

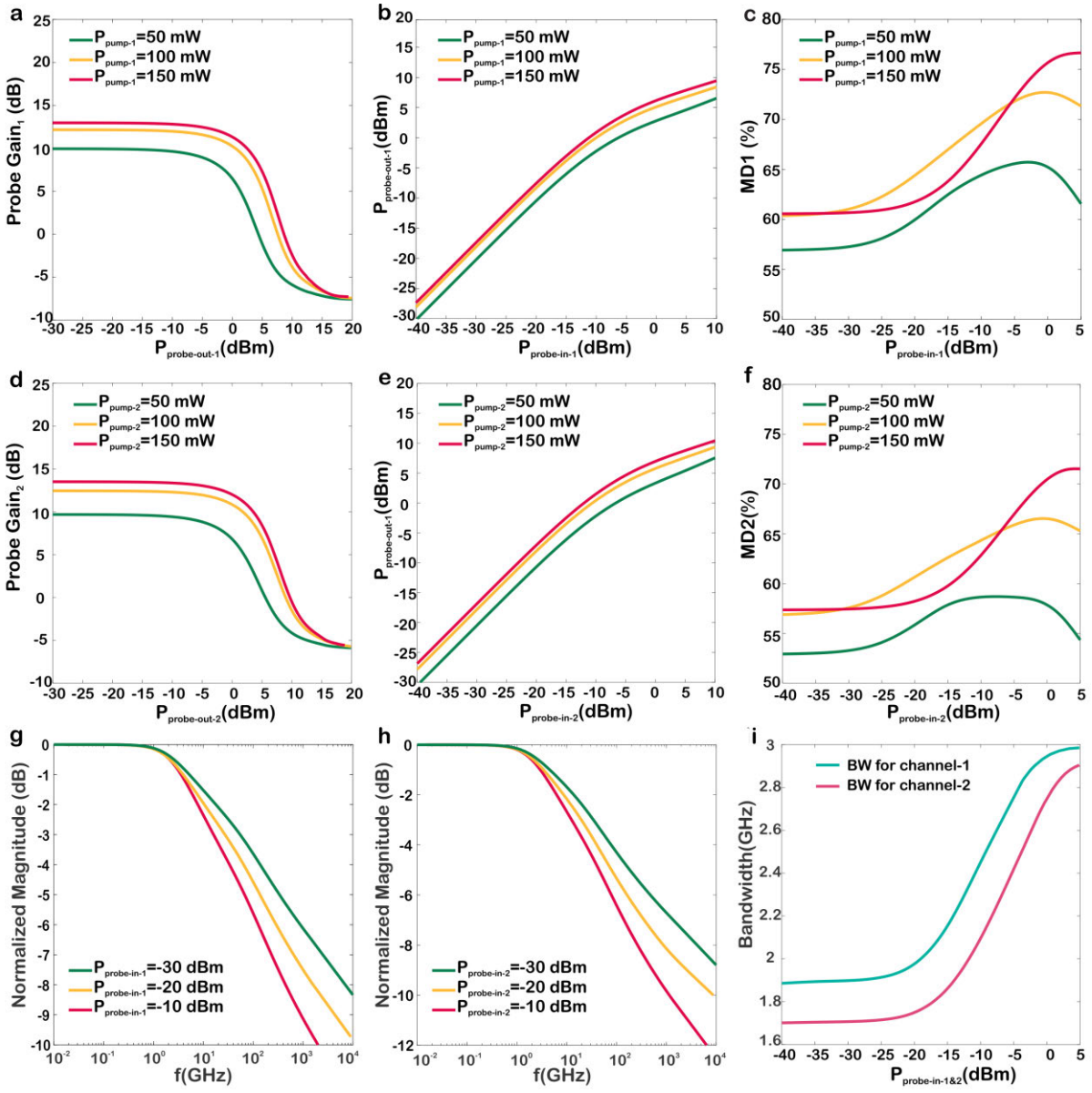

FIGURE 4. (a) The PG versus output probe power of channel-1 at the input pump power of 100 mW for channel-2. (b) The output probe power versus input probe power of channel-1 at the input pump power of 100 mW for channel-2. (c) The MD versus input probe power of channel-1 at the input pump power of 100 mW for channel-2. (d) The PG versus output probe power of channel-2 at the input pump power of 100 mW for channel-1. (e) The output probe power versus input probe power of channel-2 at the input pump power of 100 mW for channel-1. (f) The MD versus input probe power of channel-2 at the input pump power of 100 mW for channel-1. Frequency response for (g) channel-1 and (h) channel-2. (i) The bandwidth of the device versus input probe power of channel-1&2 at the input pump power of 100 mW.

from the creation of unwanted photons through spontaneous recombination is reduced. In this case, more time and more carriers are available for performing stimulated recombination in response to the CW probe signal. As a result, upon applying a Gaussian pulse to turn off the pump power, the minimum value of the output probe power decreases, leading to a reduction in MD. Figure 6 (e, f) further reveals that an increase in carrier lifetime results in an extended recovery time for carriers, ultimately leading to a decrease in the bandwidth of the device, as evidenced in Figure 6 (c).

IV. FABRICATION FEASIBILITY OF THE TWO-CHANNEL QD-AOM

In this section, a feasibility analysis of constructing the QD-AOM is presented, and practical limitations are discussed. These insights aim to provide a clear understanding of the viability of the proposed structure.

To implement the proposed modulator, the utilization of slab waveguide is recommended. A slab waveguide, also known as a planar waveguide, is a fundamental optical structure designed to confine and guide light in a single spatial dimension while allowing propagation in the other

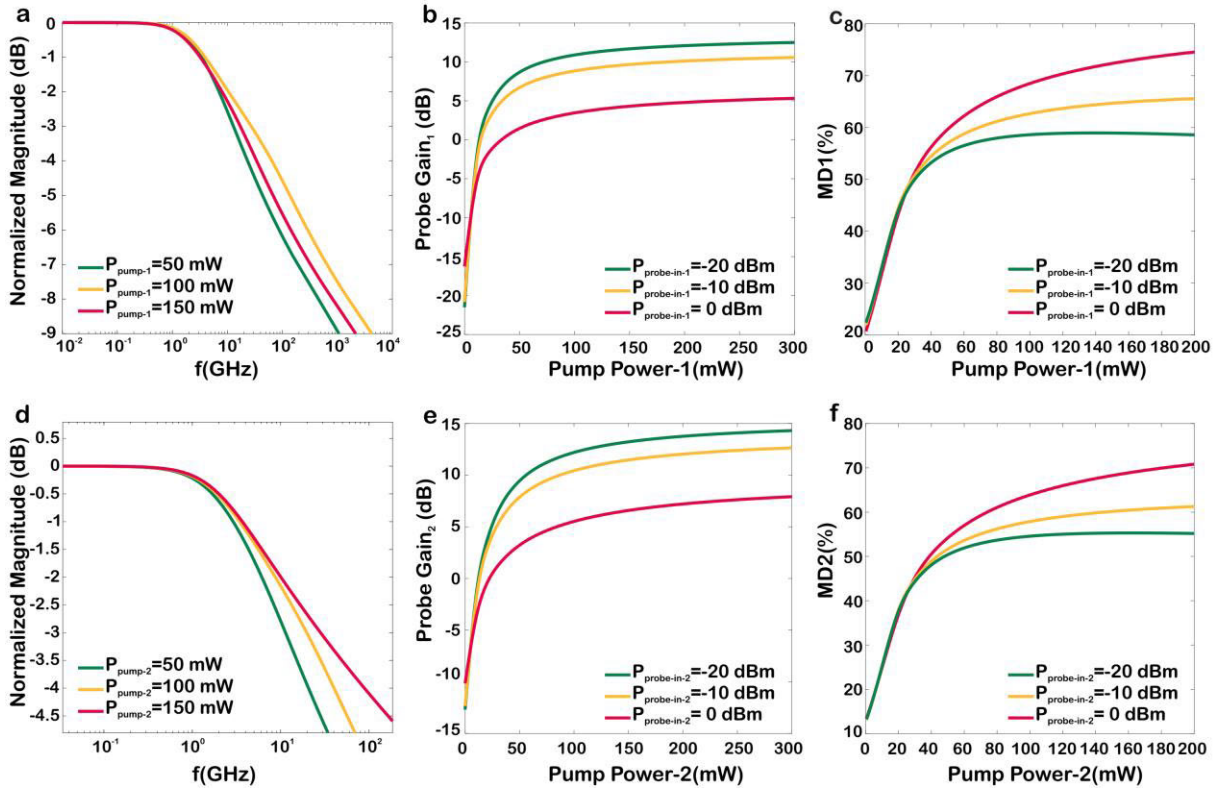

FIGURE 5. (a) Frequency response of channel-1 for the input pump power of 50 mW, 100 mW, and 150 mW. (b) The PG of channel-1 versus the pump power for the input probe power of −20 dBm, −10 dBm, and 0 dBm. (c) MD of channel-1 versus the pump power for the input probe power of −20 dBm, −10 dBm, and 0 dBm. (d) Frequency response of channel-2 for the input pump power of 50 mW, 100 mW, and 150 mW. (e) The PG of channel-2 versus the pump power for the input probe power of −20 dBm, −10 dBm, and 0 dBm. (f) MD of channel-2 versus the pump power for the input probe power of −20 dBm, −10 dBm, and 0 dBm.

two dimensions. This is achieved by sandwiching a thin dielectric core layer with a higher refractive index between two cladding layers of lower refractive indices, ensuring total internal reflection within the core. Slab waveguides are essential in numerous applications, including optical communications for data transmission, sensors for biosensing and chemical detection, and various photonic devices like lasers and modulators. Their ability to precisely confine light makes them pivotal in the development and miniaturization of integrated optical circuits [59].

In our proposed device, the active layer's refractive index surpasses that of the transmission layers, facilitating effective light confinement within the active region strategically positioned between two regions—air and glass. This positioning leverages their low refractive indices to enhance light confinement within the active region. The dimensions of our slab waveguide are chosen to optimize its function as an AOM. The proposed length and width are thoughtfully selected to ensure optimal interaction with incoming light and significant interaction with the carriers along the QD-AOM length. Based on experimental studies, it has been found that the colloidal synthesis method has the potential to fabricate samples with an active region thickness exceeding 10 μm and may even achieve a thickness of up to 20 μm [60].

The solution process in optoelectronics and photonics is rapidly advancing for implementing QDs in commercial devices. Chemical synthesis techniques regulate nanoparticle size by adjusting factors such as concentration, temperature, pH, and solvent rotation, resulting in crystals with precise diameters. Low concentrations yield uniform and precise QDs, while high concentrations can lead to poor size control. InAs nanocrystalline QDs can be made from tris(trimethylsilyl)arsine ($As[TMS]_3$), and $InCl_3$, with size regulated by growth time and infusions in an inert atmosphere. However, low input material concentration and slow reaction speed can limit nanoparticle distribution. Toluene/methanol can improve size control, and electrophoresis separates QDs of varying sizes for a narrow distribution using conventional synthesis methods [61], [62], [63]. Remarkably, QDs can be synthesized with a precision of approximately 0.1 nm [42], [44], [64], [65], [66], [67], [68].

InAs QDs have garnered significant attention from researchers due to their potential applications in photonics, optoelectronics, and biomedicine. Substantial progress has been made in refining their manufacturing processes and surface reactions. However, the challenge of upscaling these materials for commercial use persists. Ongoing research endeavors aim to surmount these barriers. For instance, recent

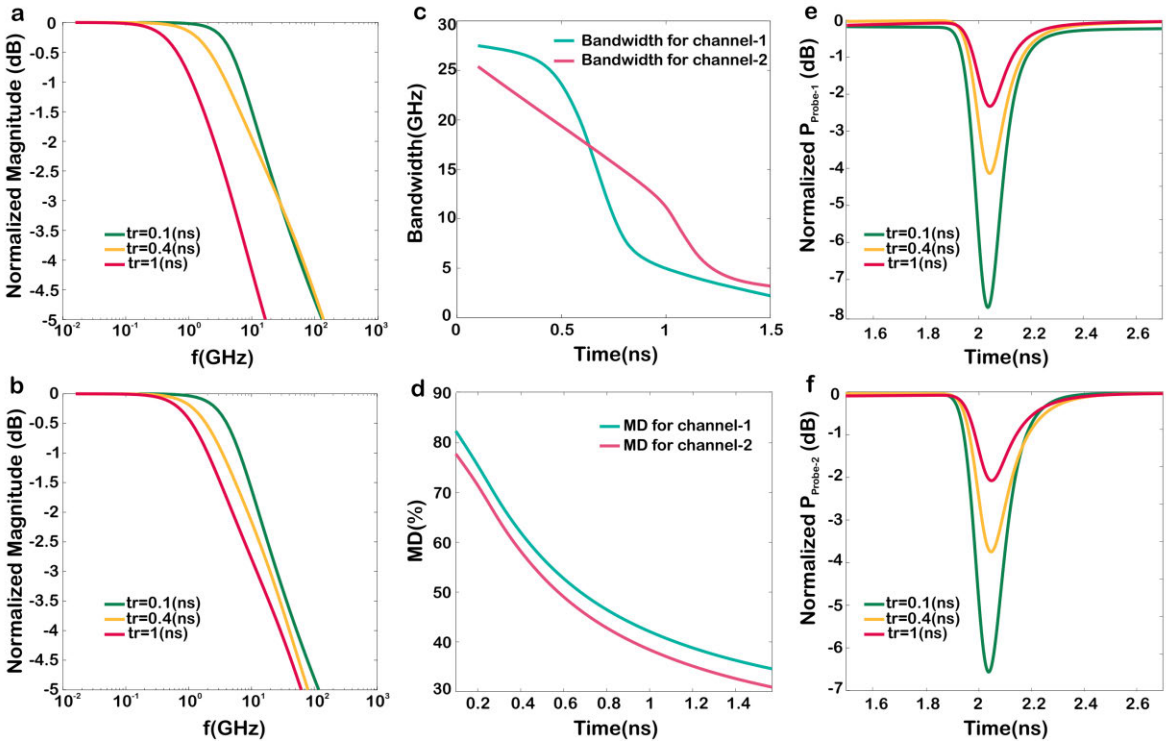

FIGURE 6. Frequency response for different lifetimes of 0.1 ns, 0.4 ns, and 1 ns (a) for channel-1 and (b) for channel-2. (c) Bandwidth of the structure versus carrier lifetime for channel-1&2. (d) MD versus carrier lifetime for channel-1&2. Normalized output probe power for different lifetimes of 0.1 ns, 0.4 ns, and 1 ns (e) for channel-1 and (f) for channel-2.

discussions on novel chemical strategies have contributed to the advancement of InAs QD synthesis, reflecting the proactive efforts of the scientific community to render these materials more suitable for large-scale applications. Furthermore, the emphasis on Restriction of Hazardous Substances (RoHS) compliance and the quest for safer alternatives to toxic elements (such as lead and mercury) underscore a steadfast commitment to achieving commercial feasibility [69].

Regarding lifetime, many studies have been done on QDs made by the solution method, and according to their application, most of these studies are on QD light-emitting diodes (QLEDs). Addressing the long-term reliability and operational lifetime of solution-processed QD devices under continuous operation and varying environmental conditions is crucial. The operating lifetime of these devices, such as QLEDs, can vary significantly. For instance, some reports indicate that QLEDs can maintain over 50% of their initial brightness for more than 4000 hours under continuous operation [70]. However, this lifetime is highly sensitive to factors such as temperature, humidity, and exposure to oxygen or light, which can accelerate degradation. Surface passivation and shell engineering are critical in enhancing the stability of InAs/AlAs core/shell QDs, mitigating degradation caused by environmental stress and continuous operation. Advances in chemical synthesis strategies, particularly in optimizing the core/shell architecture, aim to improve the long-term stability of these QDs. Careful encapsulation and the use of protective layers are essential to extend the operational lifetime by reducing the impact of environmental conditions. Nonetheless, the durability of solution-processed QD devices remains heavily dependent on the environmental protections applied during both manufacturing and usage [69], [71].

Effective coupling of pump and probe signals into two separate QD-AOM channels typically necessitates precise optical design and alignment, thereby increasing system complexity and cost. However, in our proposed model, the modulation channels are integrated, with QDs of varying radii positioned adjacently, each modulating in response to light of the corresponding wavelength. This integrated design simplifies the coupler construction and coupling process, making it more cost-effective and suitable for commercial applications.

An additional limitation in the performance of the proposed device may arise from the influence of ambient temperature and the heat generated within the modulator itself. These factors can potentially impact the device's performance, necessitating a thorough evaluation. Temperature-influenced optical characteristics are critical in optical device research. Temperature increases are correlated with increased FWHM of the homogenous broadening. While small temperature variations have negligible effects on homogenous broadening, significant widening occurs with large temperature fluctuations. Specifically, at 80 K, the FWHM is insignificant, but at 160 K, it ranges from 6–8 meV, and at 298 K, it widens further to 16–19 meV. The relationship

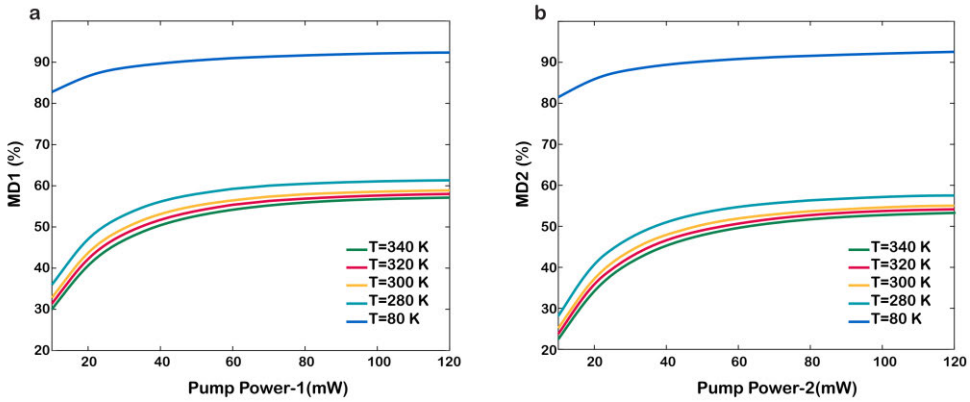

FIGURE 7. MD versus pump power for varying temperatures with an input probe power of −20 dBm (a) for channel-1 and (b) for channel-2.

between higher temperatures and increased widening is clear due to intensified interactions with phonons and other scattering processes [72].

The proportional relationship between the FWHM of the homogenous broadening at room temperature and at other temperatures can be theoretically justified by considering the temperature dependence of various broadening mechanisms in QDs. The FWHM of the homogeneous broadening Γ_{HB} in QDs is primarily influenced by two key factors: pure dephasing processes and population relaxation. These processes are known to vary with temperature, particularly due to phonon interactions. At higher temperatures, phonon interactions dominate, leading to increased dephasing and broadening. The proportionality assumption stems from the well-known temperature dependence of phonon-induced broadening, which typically follows a power-law or exponential behavior, depending on the specific phonon modes involved. As a first approximation, it is reasonable to consider that the broadening scales proportionally with the temperature-induced phonon population, which itself is proportional to the Bose-Einstein distribution [72], [73].

Experimental studies have consistently shown that the Γ_{HB} in QDs increase with temperature. For instance, in the work [73], demonstrates that the linewidth exhibits a clear temperature dependence, increasing as the temperature is raised from cryogenic levels to room temperature. This is consistent with the expected behavior due to phonon interactions. Additionally, Sugawara et al. in the reference [72], provide experimental data showing that the linewidth at room temperature can serve as a reference point for predicting the linewidth at other temperatures, further supporting the proportionality assumption. Their findings indicate that while the absolute value of the linewidth varies, the relative change with temperature remains consistent, which validates our proportionality hypothesis.

The proportional relationship between the homogeneous linewidth at room temperature and at other temperatures is grounded in the well-established temperature dependence of phonon interactions in QDs. Both theoretical considerations and experimental evidence support this assumption, confirming its scientific validity and reliability.

QD-based devices are less sensitive to temperature than bulk-based devices due to their discrete energy states, reduced carrier density during operation, and significant stability [74]. The QD-AOM proposed in this research is consistent with examples reported in recent research, demonstrating less sensitivity to temperature changes. Consequently, the QD-AOM will exhibit significant stability under operating conditions. Figure 7 illustrates the MD at five different temperatures, with the Figure 7 (a) representing channel-1 and the Figure 7 (b) representing channel-2. As mentioned, the homogeneous broadening will change with temperature change, so in this simulation, FWHMs of 1, 18, 20, 21, and 22 meV were used for temperatures of 80, 280, 300, 320, and 340 K, respectively. The figure clearly shows that at temperatures close to room temperature, the MD has little change and relatively more changes are observed at the temperature of 80 K, which is considered a low temperature. These theoretical results are completely consistent with the experimental results because the reported examples of temperature reduction increase the gain in the semiconductor optical amplifier [73], [75]. Here also, this temperature reduction increased the PG and then caused an increase in the MD.

V. CONCLUSION

In this study, we propose a novel approach to a two-channel QD-AOM utilizing a colloidal InAs/AlAs structure that can be fabricated through the solution process method. The proposed structure aims to simultaneously modulate two distinct wavelengths within the telecommunication windows (1.32 μm, 1.55 μm) by applying two pump signals with differing wavelengths (683 nm, 866 nm) through two separate channels. The modal analysis of the designed two-channel QD-AOM involves the solution of the 3D Schrödinger equation. To appraise the theoretical analysis, the coupled rate and propagation equations have been solved. Based on modeling results, channel-1 and channel-2 have MDs of 65% and 62% and bandwidths of 26.3 GHz and 19.7 GHz,

respectively, at 100 mW of the pump power and −20 dBm of the input probe power. The flexibility of the modeled two-channel QD-AOM extends to accommodating additional sizes of QDs, paving the way for multi-channel modulation. This versatility holds promising applications in diverse fields, including thermal imaging, signal processing, night vision cameras, and WDM.

REFERENCES

[1] Z. Chai, X. Hu, F. Wang, X. Niu, J. Xie, and Q. Gong, "Ultrafast all-optical switching," *Adv. Opt. Mater.*, vol. 5, no. 7, Apr. 2017, Art. no. 1600665, doi: 10.1002/adom.201600665.

[2] G. T. Reed, G. Mashanovich, F. Y. Gardes, and D. J. Thomson, "Silicon optical modulators," *Nature Photon.*, vol. 4, no. 8, pp. 518–526, Aug. 2010, doi: 10.1038/nphoton.2010.179.

[3] H. Chen, C. Wang, H. Ouyang, Y. Song, and T. Jiang, "All-optical modulation with 2D layered materials: Status and prospects," *Nanophotonics*, vol. 9, no. 8, pp. 2107–2124, Jul. 2020.

[4] D. Pacifici, H. J. Lezec, and H. A. Atwater, "All-optical modulation by plasmonic excitation of CdSe quantum dots," *Nature Photon.*, vol. 1, no. 7, pp. 402–406, Jul. 2007, doi: 10.1038/nphoton.2007.95.

[5] C. Husko, A. De Rossi, S. Combrié, Q. V. Tran, F. Raineri, and C. W. Wong, "Ultrafast all-optical modulation in GaAs photonic crystal cavities," *Appl. Phys. Lett.*, vol. 94, no. 2, Jan. 2009, Art. no. 021111, doi: 10.1063/1.3068755.

[6] H. Takeda, "All-optical modulation and amplification resulting from population inversion in two-level systems using a photonic-crystal cavity," *Phys. Rev. A, Gen. Phys.*, vol. 86, no. 1, Jul. 2012, Art. no. 013803, doi: 10.1103/physreva.86.013803.

[7] X. Zhou and J. Yu, "Multi-level, multi-dimensional coding for high-speed and high-spectral-efficiency optical transmission," *J. Lightw. Technol.*, vol. 27, no. 16, pp. 3641–3653, Aug. 2009.

[8] P. J. Winzer and R.-J. Essiambre, "Advanced optical modulation formats," in *Optical Fiber Telecommunications V B*. Amsterdam, The Netherlands: Elsevier, 2008, pp. 23–93.

[9] Y. Zhan, M. Zhang, M. Liu, L. Liu, and X. Chen, "All-optical format conversion of NRZ-OOK to QPSK and 16QAM signals via XPM in a SOA-MZI," *Chin. Opt. Lett.*, vol. 11, no. 3, 2013, Art. no. 030604.

[10] R. W. Tkach, "Scaling optical communications for the next decade and beyond," *Bell Labs Tech. J.*, vol. 14, no. 4, pp. 3–9, Winter 2010.

[11] C. Sun et al., "Single-chip microprocessor that communicates directly using light," *Nature*, vol. 528, no. 7583, pp. 534–538, Dec. 2015.

[12] A. Samani, E. El-Fiky, M. Osman, D. Patel, R. Li, M. Jacques, and D. Plant, "180 Gb/s single carrier single polarization 16-QAM transmission using an O-band silicon photonic IQM," *Opt. Exp.*, vol. 27, no. 10, p. 14447, 2019.

[13] E. L. Wooten, K. M. Kissa, A. Yi-Yan, E. J. Murphy, D. A. Lafaw, P. F. Hallemeier, D. Maack, D. V. Attanasio, D. J. Fritz, G. J. McBrien, and D. E. Bossi, "A review of lithium niobate modulators for fiber-optic communications systems," *IEEE J. Sel. Topics Quantum Electron.*, vol. 6, no. 1, pp. 69–82, Jan. 2000.

[14] Y. Ogiso, J. Ozaki, Y. Ueda, H. Wakita, M. Nagatani, H. Yamazaki, M. Nakamura, T. Kobayashi, S. Kanazawa, T. Fujii, Y. Hashizume, H. Tanobe, N. Nunoya, M. Ida, Y. Miyamoto, and M. Ishikawa, "Ultra-high bandwidth InP IQ modulator for beyond 100-GBd transmission," in *Proc. Opt. Fiber Commun. Conf. Exhib. (OFC)*. Washington, DC, USA: Optica Publishing, Mar. 2019, pp. 1–3, paper M2F-2.

[15] H. Dortaj and S. Matloub, "Two-wavelength quantum dot mid-infrared photodetectors using solution process method," in *Proc. 5th Iranian Int. Conf. Microelectron. (IICM)*, Oct. 2023, pp. 31–35.

[16] M. Mohamadzadeh, S. Matloub, and M. Faraji, "Simulation and design of dual-wavelength all-optical semiconductor optical amplifier with solution-processed quantum dots," *Opt. Mater.*, vol. 150, Apr. 2024, Art. no. 115230.

[17] Z.-B. Liu, M. Feng, W.-S. Jiang, W. Xin, P. Wang, Q.-W. Sheng, Y.-G. Liu, D. N. Wang, W.-Y. Zhou, and J.-G. Tian, "Broadband all-optical modulation using a graphene-covered-microfiber," *Laser Phys. Lett.*, vol. 10, no. 6, Jun. 2013, Art. no. 065901, doi: 10.1088/1612-2011/10/6/065901.

[18] W. Li, B. Chen, C. Meng, W. Fang, Y. Xiao, X. Li, Z. Hu, Y. Xu, L. Tong, H. Wang, W. Liu, J. Bao, and Y. R. Shen, "Ultrafast all-optical graphene modulator," *Nano Lett.*, vol. 14, no. 2, pp. 955–959, Feb. 2014, doi: 10.1021/nl404356t.

[19] Y. He, N. Li, Y. Feng, X. Li, D. Liu, J. Huang, R. Zhou, M. Wu, L. Miao, and C. Zhao, "Broadband nonlinear optical modulator with 2D organic-inorganic hybrid perovskite nanocrystals," *IEEE J. Sel. Topics Quantum Electron.*, vol. 29, no. 6, pp. 1–8, Nov. 2023.

[20] L. Wu, X. Jiang, J. Zhao, W. Liang, Z. Li, W. Huang, Z. Lin, Y. Wang, F. Zhang, S. Lu, Y. Xiang, S. Xu, J. Li, and H. Zhang, "MXene-based nonlinear optical information converter for all-optical modulator and switcher," *Laser Photon. Rev.*, vol. 12, no. 12, pp. 1–10, Dec. 2018, doi: 10.1002/lpor.201800215.

[21] H. Ahmad, A. A. Kamely, M. K. A. Zaini, M. Z. Samion, A. K. Zamzuri, and K. Thambiratnam, "1.5 and 2.0 μm all-optical modulators based on niobium-carbide (Nb2C)-PVA film," *Laser Phys. Lett.*, vol. 18, no. 8, Jul. 2021, Art. no. 085103, doi: 10.1088/1612-202x/ac0e3c.

[22] L. Shen, N. Healy, C. J. Mitchell, J. S. Penades, M. Nedeljkovic, G. Z. Mashanovich, and A. C. Peacock, "Mid-infrared all-optical modulation in low-loss germanium-on-silicon waveguides," *Opt. Lett.*, vol. 40, no. 2, p. 268, 2015, doi: 10.1364/ol.40.000268.

[23] A. Honardoost, K. Abdelsalam, and S. Fathpour, "Rejuvenating a versatile photonic material: Thin-film lithium niobate," *Laser Photon. Rev.*, vol. 14, no. 9, Sep. 2020, Art. no. 2000088.

[24] P. Kharel, C. Reimer, K. Luke, L. He, and M. Zhang, "Breaking voltage–bandwidth limits in integrated lithium niobate modulators using micro-structured electrodes," *Optica*, vol. 8, no. 3, pp. 357–363, 2021.

[25] M. Xu, M. He, H. Zhang, J. Jian, Y. Pan, X. Liu, L. Chen, X. Meng, H. Chen, Z. Li, X. Xiao, S. Yu, S. Yu, and X. Cai, "High-performance coherent optical modulators based on thin-film lithium niobate platform," *Nature Commun.*, vol. 11, no. 1, p. 3911, Aug. 2020.

[26] F. A. Juneghani, M. G. Vazimali, J. Zhao, X. Chen, S. T. Le, H. Chen, E. Ordouie, N. K. Fontaine, and S. Fathpour, "Thin-film lithium niobate optical modulators with an extrapolated bandwidth of 170 GHz," *Adv. Photon. Res.*, vol. 4, no. 1, Jan. 2023, Art. no. 2200216.

[27] S. Matloub, P. Amini, and A. Rostami, "Switchable multi-color solution-processed QD-laser," *Sci. Rep.*, vol. 10, no. 1, pp. 1–14, Mar. 2020, doi: 10.1038/s41598-020-60859-w.

[28] H. Dortaj, M. Dolatyari, A. Zarghami, F. Alidoust, A. Rostami, S. Matloub, and R. Yadipour, "High-speed and high-precision PbSe/PbI_2 solution process mid-infrared camera," *Sci. Rep.*, vol. 11, no. 1, p. 1533, Jan. 2021, doi: 10.1038/s41598-020-80847-4.

[29] S. Matloub, A. Eftekhari, and A. Rostami, "Highly ultra-broadband QD-SOA exploiting superimposition of quantum dots," *J. Mod. Opt.*, vol. 69, no. 2, pp. 92–102, Jan. 2022, doi: 10.1080/09500340.2021.2002449.

[30] C. Zhang, F. Zhang, T. Zhu, A. Cheng, J. Xu, Q. Zhang, S. E. Mohney, R. H. Henderson, and Y. A. Wang, "Two-photon-pumped lasing from colloidal nanocrystal quantum dots," *Opt. Lett.*, vol. 33, no. 21, pp. 2437–2439, 2008.

[31] N. Taghipour, I. Tanriover, M. Dalmases, G. L. Whitworth, C. Graham, A. Saha, O. Özdemir, B. Kundu, V. Pruneri, K. Aydin, and G. Konstantatos, "Ultra-thin infrared optical gain medium and optically-pumped stimulated emission in PbS colloidal quantum dot LEDs," *Adv. Funct. Mater.*, vol. 32, no. 27, Jul. 2022, Art. no. 2200832.

[32] X. Xu and X. Li, "Enhanced emission of charged-exciton polaritons from colloidal quantum dots on a SiN/SiO_2 slab waveguide," *Sci. Rep.*, vol. 5, no. 1, p. 9760, May 2015.

[33] H. Jung, M. Lee, C. Han, Y. Park, K.-S. Cho, and H. Jeon, "Efficient on-chip integration of a colloidal quantum dot photonic crystal band-edge laser with a coplanar waveguide," *Opt. Exp.*, vol. 25, no. 26, p. 32919, 2017, doi: 10.1364/oe.25.032919.

[34] S. G. Romanov, N. Vogel, K. Bley, K. Landfester, C. K. Weiss, S. Orlov, A. V. Korovin, G. P. Chuiko, A. Regensburger, A. S. Romanova, A. Kriesch, and U. Peschel, "Probing guided modes in a monolayer colloidal crystal on a flat metal film," *Phys. Rev. B, Condens. Matter*, vol. 86, no. 19, Nov. 2012, Art. no. 195145, doi: 10.1103/physrevb.86.195145.

[35] V. Sharma, B. Lovkesh, and S. Singh, "340 Gb/s all-optical NOT, XOR, XNOR, $A^{-}B$, AB^{-}, OR and NOR logic gates based on cross-gain modulation in semiconductor optical amplifiers," *Optik*, vol. 247, Dec. 2021, Art. no. 168016, doi: 10.1016/j.ijleo.2021.168016.

[36] K. Elhachemi, R. Naoum, D. Vigneswaran, and R. Maheswar, "Performance evaluation of all-optical NOT, XOR, NOR, and XNOR logic gates based on 2D nonlinear resonant cavity photonic crystals," *Opt. Quantum Electron.*, vol. 53, no. 12, p. 701, Dec. 2021, doi: 10.1007/s11082-021-03354-4.

[37] H. Dortaj, M. Faraji, and S. Matloub, "High-speed and high-contrast two-channel all-optical modulator based on solution-processed CdSe/ZnS quantum dots," *Sci. Rep.*, vol. 12, no. 1, p. 12778, Jul. 2022, doi: 10.1038/s41598-022-17084-4.

[38] P. Bhattacharya, *Semiconductor Optoelectronic Devices*. Upper Saddle River, NJ, USA: Prentice-Hall, 1997.

[39] S.-D. Chen, Y.-Y. Chen, and S.-C. Lee, "Cap layer induced stress in InAs/(Al)GaAs quantum dots," *J. Vac. Sci. Technol. B, Microelectron. Nanometer Struct. Process., Meas., Phenomena*, vol. 23, no. 5, pp. 2132–2136, Sep. 2005, doi: 10.1116/1.2052710.

[40] Q. Guo, C. K. Ong, H. C. Poon, and Y. P. Feng, "Calculation of electron effective masses in AlAs," *Phys. Status Solidi Basic Res.*, vol. 197, no. 1, pp. 111–117, Sep. 1996, doi: 10.1002/pssb.2221970117.

[41] S. Alla, R. M. Vedam, and G. V. Raghavalah, "Research in physical properties of $Al_xGa_{1-x}As$ III–V arsenide ternary semiconductor alloys," *Int. J. Phys. Sci.*, vol. 9, no. 12, pp. 281–291, Jun. 2014, doi: 10.5897/ijps2013.3838.

[42] R. Debnath, O. Bakr, and E. H. Sargent, "Solution-processed colloidal quantum dot photovoltaics: A perspective," *Energy Environ. Sci.*, vol. 4, no. 12, pp. 4870–4881, Nov. 2011, doi: 10.1039/c1ee02279b.

[43] M. Yuan, M. Liu, and E. H. Sargent, "Colloidal quantum dot solids for solution-processed solar cells," *Nature Energy*, vol. 1, no. 3, pp. 1–9, Feb. 2016, doi: 10.1038/nenergy.2016.16.

[44] F. P. G. de Arquer, A. Armin, P. Meredith, and E. H. Sargent, "Solution-processed semiconductors for next-generation photodetectors," *Nature Rev. Mater.*, vol. 2, no. 3, pp. 1–17, Jan. 2017, doi: 10.1038/natrevmats.2016.100.

[45] H. G. Yousefabad, S. Matloub, and A. Rostami, "Ultra-broadband optical gain engineering in solution-processed QD-SOA based on superimposed quantum structure," *Sci. Rep.*, vol. 9, no. 1, pp. 1–11, Sep. 2019, doi: 10.1038/s41598-019-49369-6.

[46] K. Safari Anzabi, A. Habibzadeh-Sharif, M. J. Connelly, and A. Rostami, "Wideband steady-state and pulse propagation modeling of a reflective quantum-dot semiconductor optical amplifier," *J. Lightw. Technol.*, vol. 38, no. 4, pp. 797–803, Feb. 15, 2020, doi: 10.1109/JLT.2019.2947648.

[47] J. Kim, C. Meuer, D. Bimberg, and G. Eisenstein, "Effect of inhomogeneous broadening on gain and phase recovery of quantum-dot semiconductor optical amplifiers," *IEEE J. Quantum Electron.*, vol. 46, no. 11, pp. 1670–1680, Nov. 2010, doi: 10.1109/JQE.2010.2058793.

[48] J. Kim, M. Laemmlin, C. Meuer, D. Bimberg, and G. Eisenstein, "Theoretical and experimental study of high-speed small-signal cross-gain modulation of quantum-dot semiconductor optical amplifiers," *IEEE J. Quantum Electron.*, vol. 45, no. 3, pp. 240–248, Mar. 2009, doi: 10.1109/JQE.2008.2010881.

[49] H. Dortaj and S. Matloub, "Design and simulation of two-color mid-infrared photoconductors based on intersubband transitions in quantum structures," *Phys. E, Low-Dimensional Syst. Nanostruct.*, vol. 148, Apr. 2023, Art. no. 115660.

[50] F. Demangeot, D. Simeonov, A. Dussaigne, R. Butté, and N. Grandjean, "Homogeneous and inhomogeneous linewidth broadening of single polar GaN/AlN quantum dots," *Phys. Status Solidi C*, vol. 6, no. S2, pp. S598–S601, Jun. 2009, doi: 10.1002/pssc.200880971.

[51] J. Jasieniak, L. Smith, J. van Embden, P. Mulvaney, and M. Califano, "Re-examination of the size-dependent absorption properties of CdSe quantum dots," *J. Phys. Chem. C*, vol. 113, no. 45, pp. 19468–19474, Nov. 2009, doi: 10.1021/jp906827m.

[52] J. R. Lakowicz, *Principles of Fluorescence Spectroscopy*. Springer, 2006, pp. 1–954, doi: 10.1007/978-0-387-46312-4.

[53] K. Sebald, P. Michler, J. Gutowski, R. Kröger, T. Passow, M. Klude, and D. Hommel, "Optical gain of CdSe quantum dot stacks," *Phys. Status Solidi Appl. Res.*, vol. 190, no. 2, pp. 593–597, 2002, doi: 10.1002/1521-396X(200204)190:2<593::AID-PSSA593>3.0.CO;2-4.

[54] D. Bimberg, M. Grundmann, and N. N. Ledentsov, *Quantum Dot Heterostructures*. Hoboken, NJ, USA: Wiley, 1999. Accessed: Jan. 27, 2022. [Online]. Available: https://www.wiley.com/en-ie/Quantum+Dot+Heterostructures-p-9780471973881

[55] A. Shen, J.-G. Provost, A. Akrout, B. Rousseau, F. Lelarge, O. Legouezigou, F. Pommereau, F. Poingt, L. Legouezigou, G.-H. Duan, and A. Ramdane, "Low confinement factor quantum dash (QD) mode-locked Fabry–Pérot (FP) laser diode for tunable pulse generation," in *Proc. OFC/NFOEC Conf. Opt. Fiber Commun./Nat. Fiber Optic Engineers Conf.*, Feb. 2008, pp. 25–27, doi: 10.1109/ofc.2008.4528481.

[56] S. M. Izadyar, M. Razaghi, and A. Hassanzadeh, "Quantum dot semiconductor optical amplifier: Investigation of ultra-fast cross gain modulation in the presence of a second excited state," *J. Phys. D, Appl. Phys.*, vol. 53, no. 35, Aug. 2020, Art. no. 355108.

[57] M. Sugawara, N. Hatori, H. Ebe, M. Ishida, Y. Arakawa, T. Akiyama, K. Otsubo, and Y. Nakata, "Modeling room-temperature lasing spectra of 1.3-μm self-assembled InAs/GaAs quantum-dot lasers: Homogeneous broadening of optical gain under current injection," *J. Appl. Phys.*, vol. 97, no. 4, Feb. 2005, Art. no. 043523, doi: 10.1063/1.1849426.

[58] C. Meuer, J. Kim, M. Laemmlin, S. Liebich, G. Eisenstein, R. Bonk, T. Vallaitis, J. Leuthold, A. Kovsh, I. Krestnikov, and D. Bimberg, "High-speed small-signal cross-gain modulation in quantum-dot semiconductor optical amplifiers at 1.3 μm," *IEEE J. Sel. Topics Quantum Electron.*, vol. 15, no. 3, pp. 749–756, May 2009, doi: 10.1109/JSTQE.2009.2012395.

[59] C. Waltermann, J. Koch, M. Angelmahr, J. Burgmeier, M. Thiel, and W. Schade, *Planar Waveguides and Other Confined Geometries: Theory, Technology, Production, and Novel Applications*. Germany: Springer, 2015.

[60] F. Li, C. Chen, S. Lu, X. Chen, W. Liu, K. Weng, Z. Fu, D. Liu, L. Zhang, H. Abudukeremu, L. Lin, Y. Wang, M. Zhong, H. Zhang, and J. Li, "Direct patterning of colloidal nanocrystals via thermally activated ligand chemistry," *ACS Nano*, vol. 16, no. 9, pp. 13674–13683, Sep. 2022, doi: 10.1021/acsnano.2c04033.

[61] P. Yu, M. C. Beard, R. J. Ellingson, S. Ferrere, C. Curtis, J. Drexler, F. Luiszer, and A. J. Nozik, "Absorption cross-section and related optical properties of colloidal InAs quantum dots," *J. Phys. Chem. B*, vol. 109, no. 15, pp. 7084–7087, Apr. 2005.

[62] Y. Cao and U. Banin, "Growth and properties of semiconductor core/shell nanocrystals with InAs cores," *J. Amer. Chem. Soc.*, vol. 122, no. 40, pp. 9692–9702, Oct. 2000.

[63] W.-M. Hwang, C.-Y. Lee, D.-W. Boo, and J.-G. Choi, "Separation of nanoparticles in different sizes and compositions by capillary electrophoresis," *Bull. Korean Chem. Soc.*, vol. 24, no. 5, pp. 684–686, 2003.

[64] W.-K. Koh, S. H. Choi, Y. Kim, H. Kim, K. K. Kim, and S. Jeong, "Energetic sulfide vapor-processed colloidal InAs quantum dot solids for efficient charge transport and photoconduction," *Adv. Photon. Res.*, vol. 3, no. 2, Feb. 2022, Art. no. 2100243, doi: 10.1002/adpr.202100243.

[65] J. Kim, B. K. Jung, S. Kim, K. Yun, J. Ahn, S. Oh, M. Jeon, T. Lee, S. Kim, N. Oh, S. J. Oh, and T. Seong, "Ultrasensitive near-infrared InAs colloidal quantum dot-ZnON hybrid phototransistor based on a gradated band structure," *Adv. Sci.*, vol. 10, no. 18, pp. 1–11, Jun. 2023, doi: 10.1002/advs.202207526.

[66] S. Kim, S. Yeon, M. Lee, J. Jin, S. Shin, N. Gwak, I. Jeong, H. Jang, G. W. Hwang, and N. Oh, "Chemically and electronically active metal ions on InAs quantum dots for infrared detectors," *NPG Asia Mater.*, vol. 15, no. 1, May 2023, Art. no. 30, doi: 10.1038/s41427-023-00477-w.

[67] M. Liu, Y. Chen, C.-S. Tan, R. Quintero-Bermudez, A. H. Proppe, R. Munir, H. Tan, O. Voznyy, B. Scheffel, G. Walters, A. P. T. Kam, B. Sun, M.-J. Choi, S. Hoogland, A. Amassian, S. O. Kelley, F. P. G. de Arquer, and E. H. Sargent, "Lattice anchoring stabilizes solution-processed semiconductors," *Nature*, vol. 570, no. 7759, pp. 96–101, May 2019, doi: 10.1038/s41586-019-1239-7.

[68] O. Voznyy, B. R. Sutherland, A. H. Ip, D. Zhitomirsky, and E. H. Sargent, "Engineering charge transport by heterostructuring solution-processed semiconductors," *Nature Rev. Mater.*, vol. 2, no. 6, pp. 1–10, May 2017.

[69] H. B. Jalali, L. De Trizio, L. Manna, and F. Di Stasio, "Indium arsenide quantum dots: An alternative to lead-based infrared emitting nanomaterials," *Chem. Soc. Rev.*, vol. 51, no. 24, pp. 9861–9881, 2022.

[70] Y. Sun, C. Han, R. Li, C. Xiang, T. Zhang, and L. Qian, "Fully solution-processed red tandem quantum dot light-emitting diodes with an EQE exceeding 35%," *J. Mater. Chem. C*, vol. 12, no. 27, pp. 10053–10060, 2024.

[71] L. Zhang, W. Xiang, and J. Zhang, "Thick-shell core/shell quantum dots," in *Core/Shell Quantum Dots: Synthesis, Properties and Devices*. Springer, 2020, pp. 197–218.

[72] M. Sugawara, K. Mukai, Y. Nakata, H. Ishikawa, and A. Sakamoto, "Effect of homogeneous broadening of optical gain on lasing spectra in self-assembled $In_xGa_{1-x}As$/GaAs quantum dot lasers," *Phys. Rev. B, Condens. Matter*, vol. 61, no. 11, p. 7595, 2000.

[73] P. Borri, W. Langbein, S. Schneider, U. Woggon, R. L. Sellin, D. Ouyang, and D. Bimberg, "Exciton relaxation and dephasing in quantum-dot amplifiers from room to cryogenic temperature," *IEEE J. Sel. Topics Quantum Electron.*, vol. 8, no. 5, pp. 984–991, Sep. 2002.

[74] M. Sugawara, H. Ebe, N. Hatori, M. Ishida, Y. Arakawa, T. Akiyama, K. Otsubo, and Y. Nakata, "Theory of optical signal amplification and processing by quantum-dot semiconductor optical amplifiers," *Phys. Rev. B, Condens. Matter*, vol. 69, no. 23, Jun. 2004, Art. no. 235332.
[75] O. Eyal, A. Willinger, S. Banyoudeh, F. Schanbel, V. Sichkovskyi, V. Mikhelashvili, J. P. Reithmaier, and G. Eisenstein, "Static and dynamic characteristics of an InAs/InP quantum-dot optical amplifier operating at high temperatures," *Opt. Exp.*, vol. 25, no. 22, pp. 27262–27269, 2017.

MOHAMMAD FARAJI received the B.Sc. degree in electronics and electrical engineering from the University of Mohaghegh Ardabili, Ardabil, Iran, in 2018, and the M.S. degree in micro and nanodevices in electronic engineering from the University of Tabriz, Tabriz, Iran, in 2022, where he is currently pursuing the Ph.D. degree in photonic/electronic engineering. His research interests include optical modulators, optical amplifiers, and optical sensors.

SAMIYE MATLOUB received the Ph.D. degree in photonic/electronic engineering from the University of Tabriz, Tabriz, Iran, in 2010. She is currently an Associate Professor of electronic engineering and photonics science with the University of Tabriz, where she also founded the Quantum Photonics Research Laboratory (QPRL). With a portfolio comprising over 50 international journals and conference papers, her scholarly contributions are noteworthy. Her research interests include optoelectronic devices and optical integrated circuits, reflecting her keen interest in advancing practical applications within the field. Her leadership at QPRL underscores her commitment to fostering innovation and driving progress in photonics research.

HANNANEH DORTAJ received the B.Sc. degree in electronics engineering and the M.Sc. degree in optoelectronics from the University of Tabriz, Iran, in 2017 and 2019, respectively. She is currently pursuing the Ph.D. degree with the University of Tabriz and the sabbatical period with Humboldt-Universität zu Berlin. Her research interests include optoelectronics, nanostructures, photonics, and optical integrated circuits.